JTTEE5 19:1186–1194
DOI: 10.1007/s11666-010-9535-7
1059-9630/$19.00 © ASM International

Microstructure and Thermal Properties of Plasma Sprayed Thermal Barrier Coatings from Nanostructured YSZ

Jing Wu, Hong-bo Guo, Le Zhou, Lu Wang, and Sheng-kai Gong

(Submitted January 29, 2010; in revised form July 4, 2010)

Nanostructured yttria-stabilized zirconia (YSZ) thermal barrier coatings (TBCs) were produced by atmospheric plasma spraying. The microstructure of the sprayed coating was characterized by transmission electron microscope (TEM) and scanning electron microscope (SEM). The nano-coating had a higher porosity of ~25% than the conventional coating, which is mainly attributed to the large amount of intersplat gaps in the nano-coating. The thermal conductivity for the nano-coating was in the level of 0.8-1.1 W/m·K, about 40% lower than that for the conventional coating, indicating a better thermal insulation performance. The nano-TBC exhibited a thermal cycling lifetime of more than 500 cycles, whereas spallation failure of the conventional TBC occurred within 200 cycles. Accelerated sintering could be one of the reasons for the failure of the nano-TBC.

Keywords Thermal barrier coatings (TBCs), Plasma spraying (PS), Nanostructure, Microstructure, Sintering

1. Introduction

Plasma sprayed yttria-stabilized zirconia (YSZ) thermal barrier coatings (TBCs) have been used in the hot section components of gas turbine engines in the past decades (Ref 1-3). Because of their low thermal conductivities at elevated temperature, YSZ TBCs effectively reduce the operating temperature and hence increase the durability of the underlying components (Ref 4-9). Traditional YSZ TBCs are usually sprayed from hollow spherical (HOSP) powders or fused and crashed (FC) powders. The thermal conductivities of the sprayed coatings are in range of 1-2 W/m·K, which are strongly dependant on the processing parameters for the coatings (Ref 10, 11). Also, the sprayed coatings can survive hundreds of cycles when subjected to thermal shock testing (Ref 11). As advanced turbine engines develop toward higher turbine inlet temperature (TIT), it is one of the biggest challenges to improve the capability of TBCs so that they can be operated in much harsher environment (Ref 12).

In recent years, more and more attentions have been focused on nanostructured materials, in order to improve the properties such as hardness, strength, ductility, and toughness (Ref 13). Nanostructure TBCs have exhibited promising potential in increasing thermal insulation property and prolonging thermal cycling lifetime when compared to conventional TBCs (Ref 14). As TBCs spall or debond under high-temperature thermal cycling conditions, thermal shock behavior is one of important indications of TBCs performances (Ref 15). As reported, the number of cycles to failure of the nanostructured YSZ coatings was approximately 2-3 times longer than that of the conventional coatings when the thermal shock test was carried out at temperatures from 1000 to 1300 °C (Ref 16). Wang et al. also compared the thermal shock performances of nanostructured and conventional TBCs by quenching tests. Under such testing condition, the thermal shock lifetime of the nanostructured coating was significantly higher than that of the conventional coating (Ref 17). A similar result was also reported by Liu et al. (Ref 15). These results have proved the higher compliance capacities of the nanostructured YSZ coatings (Ref 14).

Zhou et al. (Ref 18) investigated the effect of annealing on the growth of nanostructured TBCs and found that the grain size of the nano-coating increased with increasing of annealing temperature and time. Thermal cyclic testing result at 1100 °C showed that the nanostructured YSZ TBC exhibited an improved thermal cycling lifetime as compared to the conventional TBC (Ref 19). Lima et al. (Ref 14) have also investigated the sintering behavior and associated thermo-mechanical properties of free-standing nanostructured TBCs and discussed the effect mechanism

This article is an invited paper selected from presentations at the 4th Asian Thermal Spray Conference (ATSC 2009) and has been expanded from the original presentation. ATSC 2009 was held at Nanyang Hotel, Xi'an Jiaotong University, Xi'an, China, October 22-24, 2009, and was chaired by Chang-Jiu Li.

Jing Wu, Hong-bo Guo, Le Zhou, and **Sheng-kai Gong**, Department of Materials Science and Engineering, Beihang University, No. 37, Xueyuan Road, Beijing 100191, China and Beijing Key Laboratory for Advanced Functional Materials and China Film Technology, Beihang University, No. 37, Xueyuan Road, Beijing 100191, China; and **Lu Wang**, Department of Materials Science and Engineering, Beihang University, No. 37, Xueyuan Road, Beijing 100191, China. Contact e-mails: guo.hongbo@buaa.edu.cn and gongsk@buaa.edu.cn.

of sintering. It should be pointed out that both annealing treatment and thermal cycling testing of the nano-coatings in the above papers were performed in a uniform temperature field. There was no temperature gradient across the TBC thickness and no substrate binding up. The failure mechanism was different from those in real engine service environments.

In our article, the thermal cycling lifetime and associated failure mechanism of the TBCs sprayed from nanostructure YSZ were investigated in burner rig setup that simulated the operation condition of turbine engine. Also, thermal insulation properties of the nano- and conventional TBCs were compared. It is believed that these results are of great importance for the potential application of TBCs in turbine engines.

2. Experimental Procedures

2.1 Preparation of the Nanostructured YSZ Coating

Ni-based superalloy K3 was used as the substrate materials. 100-120 μm NiCrAlY bond coats were first sprayed onto Ni-based superalloy by HVOF. Metco 7M atmospheric plasma spray equipment with 9 MB spray pistol and METCO 4MP-DUAL type feedstock system was used to spray the nanostructured YSZ TBCs. A 7.8 wt.% Y_2O_3 and 2.6 wt.% HfO_2 stabilized nanostructured zirconia powder, was used in this study, which mostly comprises tetragonal phase with the content of more than 94%. The YSZ topcoat was sprayed to ~200 μm. For comparison, conventional YSZ TBCs with the nearly same thickness were also sprayed from commercial powder METCO® 204 NS. The processing parameters for plasma spraying (PS) of YSZ coatings are listed in Table 1. The choice of spray parameters were based on the first authors' previous work (Ref 20, 21). Under the spray condition, both the conventional and nanostructure TBCs yielded their own satisfying lifetimes when subjected to thermal shock testing.

2.2 Thermal Shock Test

Thermal shock test of the sprayed samples was performed in a gas burner test facility, as shown in Fig. 1. Disk samples (Ø 30 × 3 mm) were used for testing. The sample was heated for 20 s to the desired surface temperature of 1523 K and then held at this temperature for 10 min. During heating stage the backside of the sample was cooled by compressed air to maintain a controlled temperature gradient through the sample thickness and in this case, the substrate temperature was in a range of 1173-1273 K. During cooling stage the burner was removed from the coating surface and the sample was cooled by compressed air from both sides for 2 min. The thermal cycling lifetime is defined as the number of cycles at which spallation of more than 10% coating surface area occurs.

During thermal shock testing, the coating surface temperature was measured using a pyrometer operated at a wavelength of 8-13 μm. The measurement was calibrated in order to minimize the effect of emission and reflection. The backside temperature of the sample was also measured by a thermo-couple which was fixed to the backside of the coated sample. For both of the nanostructured coating and conventional coating samples, the coating surfaces were heated to the same temperature of about 1523 K and the backsides of the coated samples were cooled by compressed air at a nearly same cooling rate. In this case, the temperature gradients across the thickness of the samples were compared quantitatively.

Table 1 Processing parameters for plasma spraying of YSZ coatings

Power, KW	*D*, mm	Ar, slpm	H_2, slpm	*F*, g/min	*V*, mm/s
37.5	120	80	16	40	500

D spray distance, *F* feed rate, and *V* transverse speed of plasma gun

2.3 Microstructure Characterization

The microstructures of the sprayed coatings were examined by a JEM-2100F transmission electron microscopy (TEM). The morphologies of surfaces and cross sections of the coatings were investigated by a QUANTA 600 scanning electron microscopy (SEM). Phases were identified by x-ray diffraction (XRD, Rigaku Diffractometer, Cu K_α radiation). Porosities in the free-standing coating specimens were determined by a mercury porosimeter (Micromeritics Autopore II, Shimadzu, Kyoto, Japan). Rectangular specimens were used for the measurement. The measurement was made with a changing pressure from 0.004 to 400 MPa, which corresponds to pore diameters from 180 to 4 nm, respectively.

2.4 Thermo-Physical Properties

Free-standing YSZ coating specimens were produced by removing the coatings from the substrates using hydrochloric acid. Thermal diffusivity $\alpha(T)$ measurements

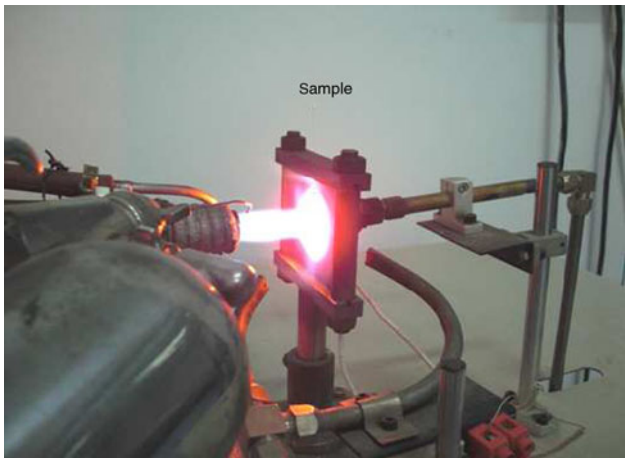

Fig. 1 Burner rig test equipment

were conducted using a laser flash device (LFA 427/7/G, Netzsch) on disk-shaped specimens of 12.6 mm in diameter and 1 mm in height. The specimens were heated from room temperature up to 1473 K. The thermal diffusivity data were recorded every 100 K. Before the measurements, the specimen surfaces were coated with a thin film of carbon to increase the absorption of laser pulses. Specific heat $C_P(T)$ measurements were performed using a differential scanning calorimeter (STA 449 C, Netzsch). Bulk densities ρ of the specimens were measured by the Archimedes technique. Thermal conductivities $K(T)$ were calculated using Eq (1):

$$K(T) = \alpha(T) \cdot C_P(T) \cdot \rho \quad \text{(Eq 1)}$$

Shrinkage of the specimens at 1523 K for 10 h was determined using a high-temperature dilatometer (Netzsch DIL 402E, Germany) on specimens of 25 mm in length and 5 mm in both width and height.

3. Results and Discussion

3.1 Feedstock Morphology

Figure 2(a) shows the morphology of the original YSZ particles for spraying nanostructure coatings. The grain sizes of the particles are between 50 and 100 nm. The powders were then agglomerated at 1173 K in order to be convenient for spraying. The agglomerated powder feedstocks are spherical, with the size of 30-100 μm, as shown in Fig. 2(b). The commercial 204 NS powder feedstocks are also featured with spherical morphology, with a similar size distribution of 20-120 μm (Ref 10, 12).

3.2 Microstructure of Sprayed Coating

Figure 3(a) shows the surface morphology of the as-sprayed nanostructured coating. Two different surface morphologies are observed. One is the dense and smooth zones, indicating good molten state of particles, the other one the rough and porous zones, indicating unmolten or semi-molten state of particles. The morphology of the cross section of the coating is shown in Fig. 3(b). The coating contains a number of porosity with the size of larger than 1 μm. A similar morphology can be also seen in the conventional coating as shown in Fig. 3(c).

Figure 4 shows the cumulative porosity distribution of the free-standing coating specimens determined by mercury porosimetry. Before the measurement, the specimen surfaces were finely polished in order to minimize the effect of surface roughness to the porosity measurement. The pores include micropores small than 1 μm in size and large defects larger than 1 μm. The nano-coating has a porosity of about 25%, while the conventional coating a relatively lower porosity of ~12%. It should be noted that both the nano- and conventional coatings show a similar level of the macro-porosity corresponding to the large defects. However, for the nano-coating the micro-porosity corresponding to the micropores is about 20%, much higher than that for the conventional coating. It has been shown that the micropores existing in the plasma sprayed YSZ coatings are mainly from intersplat gaps, resulting from poor wetting/adhesion between splats. The large defects originate partially from gas entrapment and unmelted particles. In terms of this, it can be inferred that for a given coating thickness the number of the intersplat gaps in the nano-coating is much higher than that in the conventional coating.

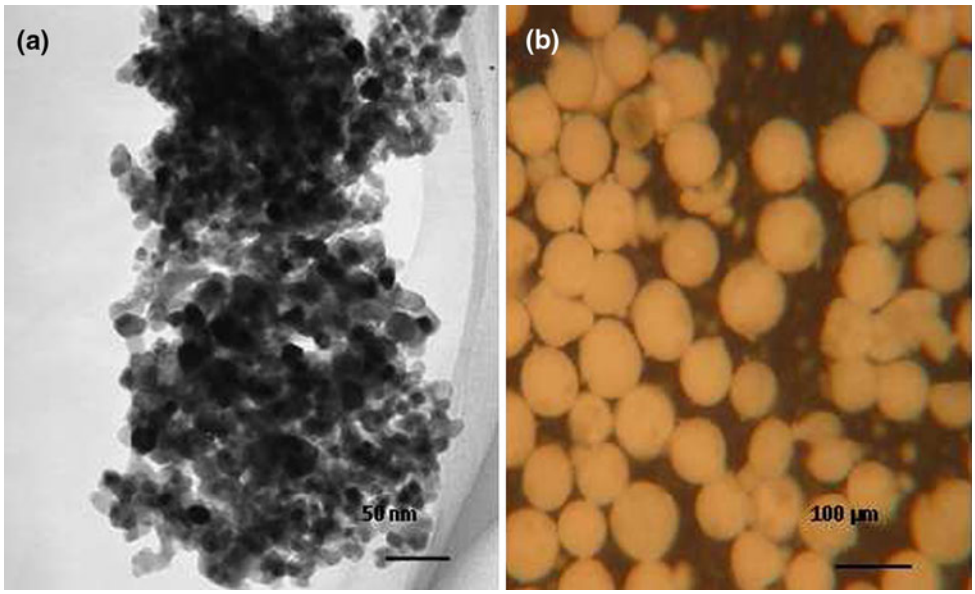

Fig. 2 (a) TEM bright-field image of nanostructure zirconia powder collected on a substrate. (b) TEM image of the agglomerated particles

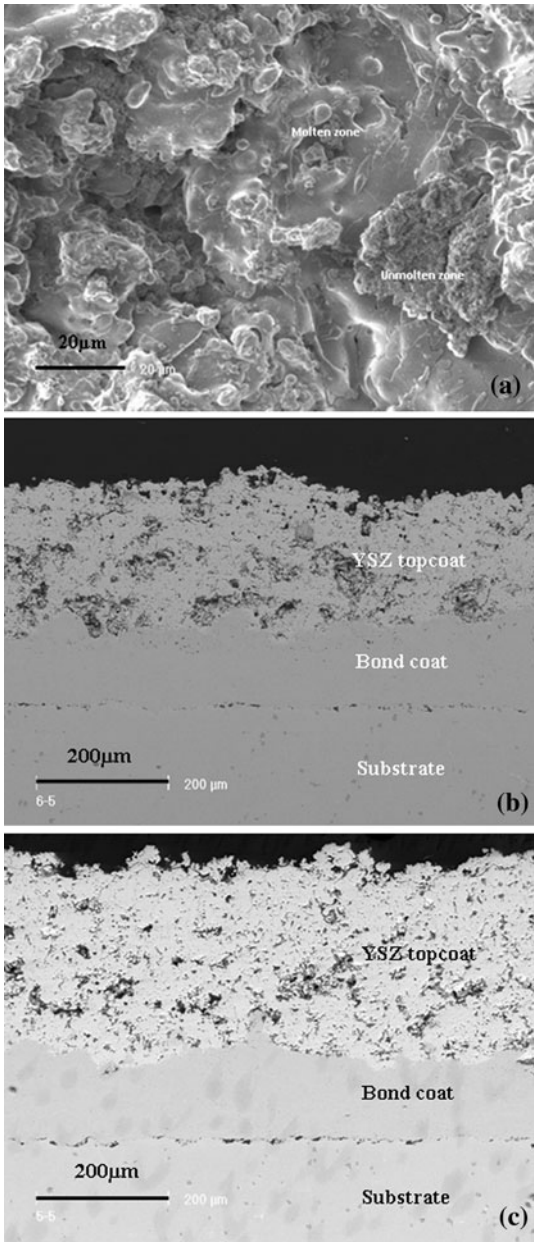

Fig. 3 The morphologies of surface (a) and cross section (b) of the nano-YSZ coating and (c) the cross section morphology of sprayed conventional YSZ coating

Figure 5(a) and (b) shows the fractural morphologies of cross sections of the conventional and nanostructured coatings, respectively. The conventional coating basically exhibits a typical splat structure (Fig. 5a), implying a good melt state, since few of granular zones were presented in the coating. The splat structure was formed by the semi-molten particles, with the splats thickness of ~10 μm. Compared to the conventional coating, the nanostructured coating reveals relatively thinner splats, with the splat thickness of ~5 μm. In addition, the splats in the nano-coating consist of columnar grains in the submicron size. It has been reported by Chen et al. that the nanocrystals

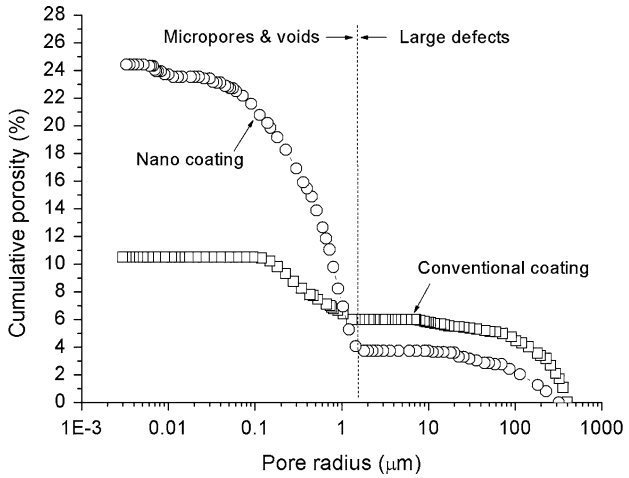

Fig. 4 Results of mercury-porosimetry measurements for sprayed YSZ coatings

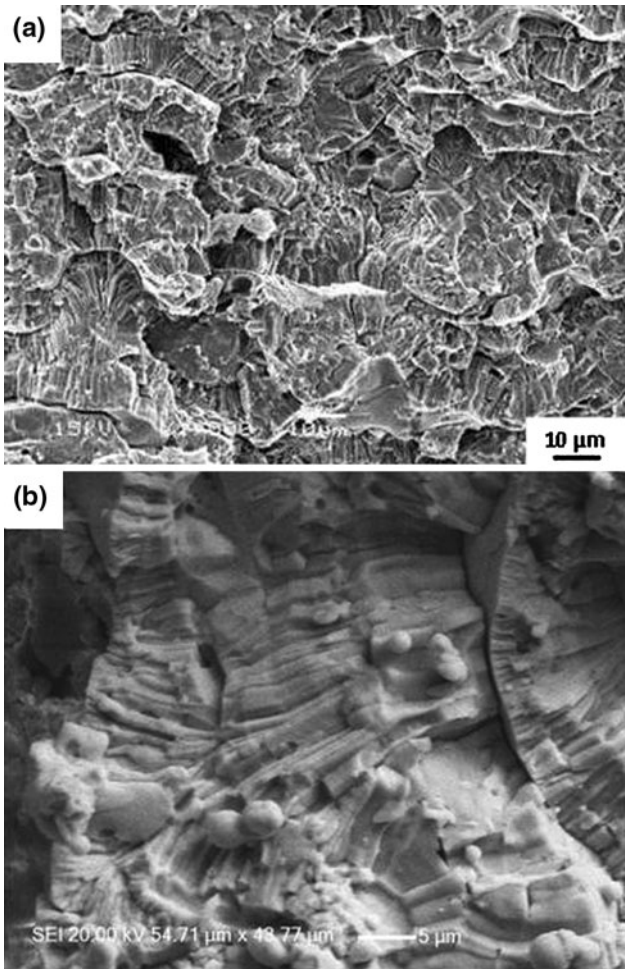

Fig. 5 SEM micrograph of fractural cross section of conventional coating (a) and TEM image of cross section of the nano-coating (b)

in the nanostructure coatings mainly come from the re-solidification of the molten and semi-molten powders (Ref 22).

It is proposed by Lima et al. that the two kinds of structures in nano-YSZ coatings maintain the coating integrity (Ref 14). The nanoparticles resulting from un-molten powders can fill in the core of the semi-molten particles in order to make the coating integrity. It is also reported in some literatures that this kind of structure decreases the cohesive strengths between lamellae (Ref 14). However, in other literatures, it is pointed out that the semi-molten nanoparticles zone is the specific structure contrary to the conventional coatings. More than 30% preserved non-molten nanoparticles in the coating exhibit higher toughness and a very low elastic modulus (Ref 23).

The high porosity of the nano-coating also contributes to lower thermal conductivity of TBC. As shown in Fig. 6(a), the values of thermal diffusivities for the nano-coating are in a range of 0.3-0.5 mm^2/s between room temperature and 1473 K, while those for the conventional coating are in the level of 0.5-0.7 mm^2/s. Specifically, the diffusivity at 1473 K that is relevant temperature for TBC application is 0.3 and 0.5 mm^2/s for the nano-coating and conventional coating, respectively. The specific heat for the conventional coating is a littler higher than that for the nano-coating, as shown in Fig. 6(b). The density of the free nano-coating specimen was measured to be 4.3 g/cm^3, while that of the free conventional coating specimen measured to be 5.5 g/cm^3. Finite element modeling has been attempted to study the effects of shape, orientation, and volumetric percentage of porosity on the thermal conductivities (Ref 24). The calculated thermal conductivity from Eq 1 is shown in Fig. 6(c). For the nano-coating, the thermal conductivity is in the level of 0.8-1.1 W/m·K, which is lowered by about 40% as compared to that of the conventional coating (about 1.6-2 W/m·K for the conventional coating). It was found that horizontal cracks, such as intersplat gaps, were particularly effective in reducing thermal conductivity as the interfaces formed by such gaps were perpendicular to the heat flux. However, cylinder-shaped pores, including vertical cracks, have little effect on the conductivity. In the present study, the porosity of the nano-coating is relatively lower than that of the conventional coating because the number of the intersplat gaps in the nano-coating is much higher than that in the conventional coating, as shown in Fig. 4. Therefore, the lower thermal conductivity of the nano-coating can be explained by its higher number of intersplat gaps.

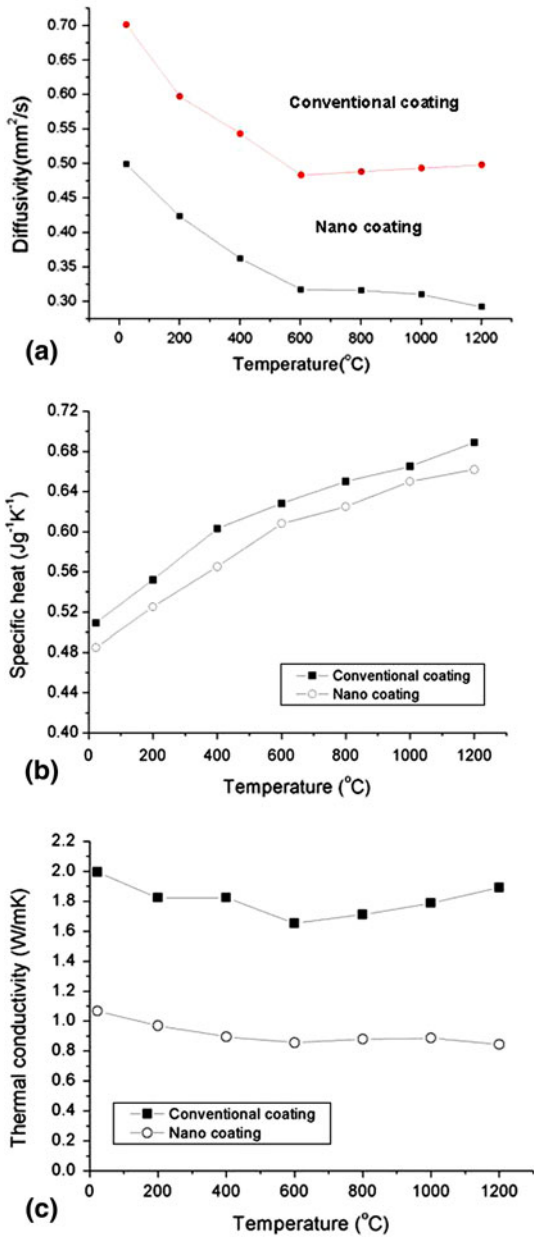

Fig. 6 Thermal diffusivities (a), specific heat (b), and thermal conductivities (c) of the sprayed conventional and nanostructured YSZ coatings

3.3 Thermal Shock Resistances of TBCs

Thermal shock tests of the coating samples were conducted on the burner rig setup. The coating surface temperatures were set to be 1523 K and the back sides of the samples were cooled by compressed air at the same cooling rate. Figure 7 compares the temperature gradients of the two coating samples. The nano-coating reveals a gradient of about 250 K, while the conventional coating a gradient of about 200 K, despite some fluctuations occurred during the measurements. As the coatings were sprayed to the nearly same thickness, it can be inferred that the nanostructure zirconia coating has a better thermal insulation property.

Spallation failure of the conventional coating occurred after around 200 cycles as shown in Fig. 8(a). Spallation of the YSZ coating started from the rim of the sample and extended to the center. This is the typical failure mechanism for TBCs, resulting from the singularity of thermal stresses at the rim (Ref 25). In contrast, the nano-YSZ coating remained intact after 500 cycles, however, large area spallation occurred after 530 cycles as shown in

Fig. 8b. In terms of the results, the nanostructured TBC revealed a better thermal shock resistance than the conventional TBC.

To investigate the failure mechanism, the cross section of the nano-coating specimen was examined. The specimen was sectioned along the white line as shown in Fig. 9(b). The YSZ coating was cracked along the interface between the ceramic coating and thermally grown oxide (TGO) as shown in Fig. 9(a). This is a typical failure mode of plasma sprayed TBCs (Ref 26, 27).

The morphologies of the TGO layers in the coatings after failure were examined. For the nano-TBC after 530 cycles thermal shock testing, the bond coat was operated at a temperature of about 1273 K for nearly 90 h. As a result, a TGO layer of nearly ~5 μm was grown on the bond coat as shown in Fig. 9(a). The TGO consists of two layers: the bottom layer (dark) and the top layer (gray). According to EDS analysis, the top layer mainly comprises spinel phases and the bottom layer α-Al_2O_3 phase. TGO layer is continuous and protective. No small cracks formed at the crests of the underlaid TGO layer. In the case of the conventional coating, the operating temperature for the bond coat could be a little higher under the nearly same coating surface temperature, due to its relatively lower thermal insulation. However, its oxidation time is no longer enough to form a thick TGO (about 30 h) shown in Fig. 9(b). Therefore, it can be inferred that for the conventional TBC the formation and growth of TGO is not the major reason for TBC spallation. The thermal stresses generated during thermal cycling could lead to failure of the TBC.

Quite different from the morphology of the as-sprayed nanostructured coatings, there are some darker zones in the coating after 530 cycles test (Fig. 10). As mentioned foregoing, the darker zones are the semi-molten agglomerated powder called ''nanozones.'' In addition, it can be

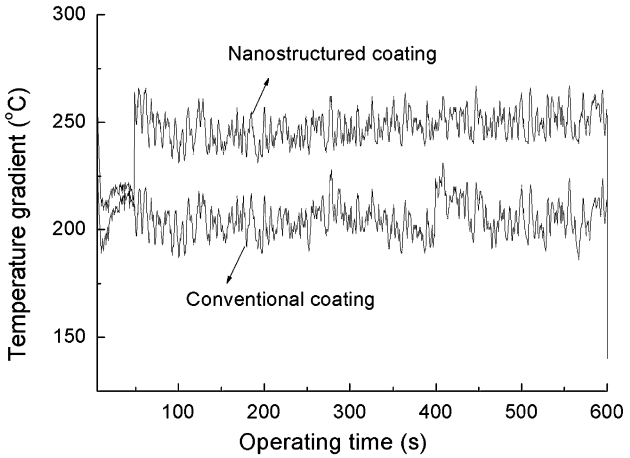

Fig. 7 Temperature gradients across the thickness of the coated specimens at one cyclic during the burner rig test, where the coating surface temperatures were set to be about 1523 K

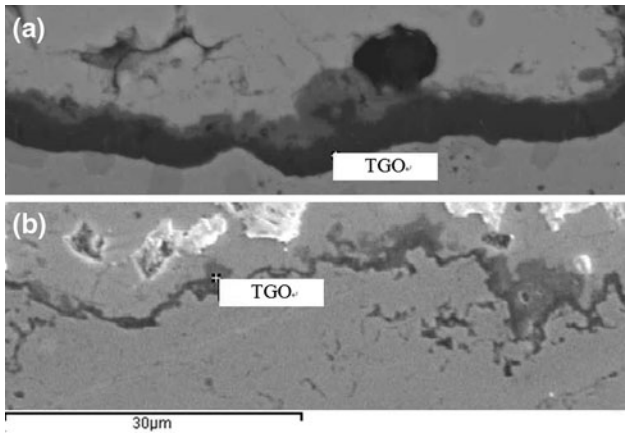

Fig. 9 SEM micrographs of cross sections of plasma sprayed TBCs after thermal shock testing: (a) nanostructured, 530 cycles and (b) conventional, 200 cycles

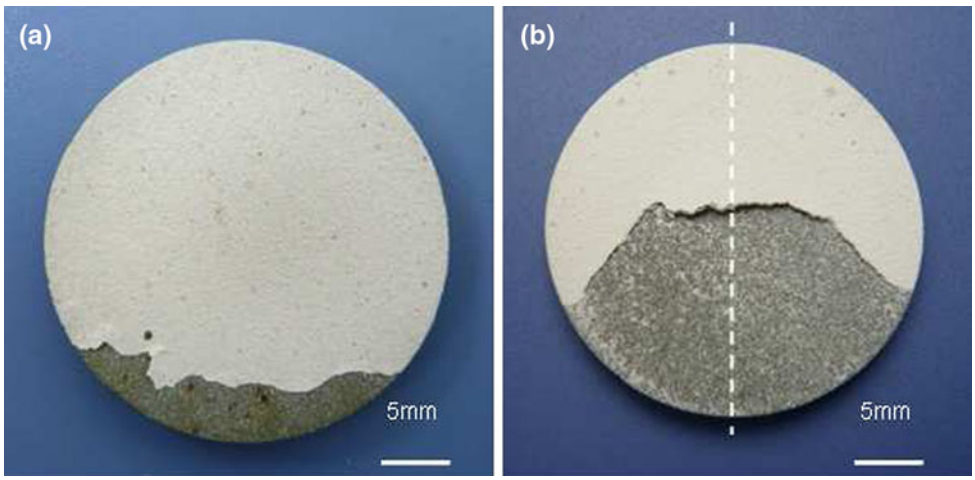

Fig. 8 Photographs of the conventional TBC after 200 cycles test (a) and the nanostructure TBC after 530 cycles test. During testing, the coating surface temperature was set to be about 1523 K

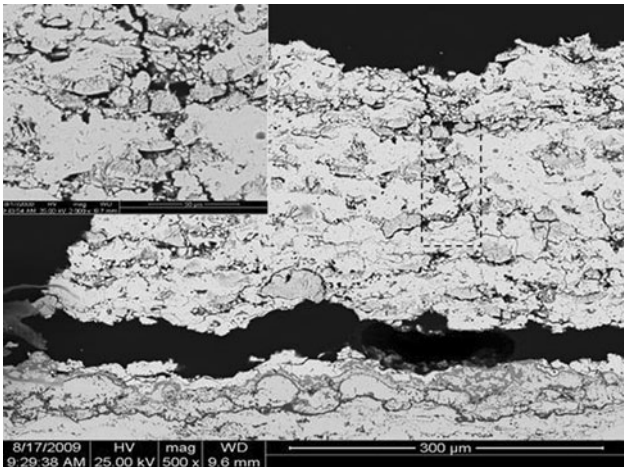

Fig. 10 Higher magnification of the area in Fig. 9(a) surrounded by the black line

observed that the darker zones surrounded by the molten zones, consist of fine particles. It is well admitted that the two structure zones have different densification rates. The molten parts were basically formed by the previously molten and currently re-solidified particles. The inner structure of the molten parts already exhibited high density after re-solidification from the molten state (Ref 14). Some voids were presented between the molten zones and the nano-zones. The numbers of coarse granules in the nanozones increased. The areas between the two parts with different sintering rates would generate the voids horizontal, when the coating exposed to high-temperature gas. According to Lima et al. (Ref 14), the healing of the fine interlamellar pores was counteracted by the formation of the horizontal voids in the nanostructured coating. Also, it has been shown by McPherson et al. that the fine pores play a major role in the mechanical and thermal properties of thermal spray coating (Ref 28). It can be hypothesized that the counteracting effect of the nanostructure coating makes it better thermal shock resistant compared to the conventional coating.

Phase transformation of YSZ TBCs often occurs during thermal cycling, which results in a volume expansion of ~5% (Ref 29). The volume expansion could cause failure of the TBCs. XRD was used for phase identification of the coatings before and after thermal shock testing. The as-sprayed coating consists of non-equilibrium tetragonal phase (t') and stable tetragonal phase with low content yttria (t) as shown in Fig. 11(a) due to fast cooling of the coating materials during PS process. Leoni et al. reported that the c-to-a axes ratio (c/a) decreases as the content of Y_2O_3 in zirconia increases. The tetragonality is defined by $c/(a\sqrt{2})$, which equals the normally given c/a. Tetragonal phases with $c/(a\sqrt{2})$ of 1.017 are considered to be the ''low-stabilizer'' tetragonal phase (t_1), those with $c/(a\sqrt{2})$ of ~1.005-1.007 to be the tetragonal t' phase, and those with $c/(a\sqrt{2})$ of 1.003 to be the ''high-stabilizer'' tetragonal 2 phase (t_2) (Ref 30). After 500 cycles testing, the coating basically consists of t', t and cubic (c) phases as

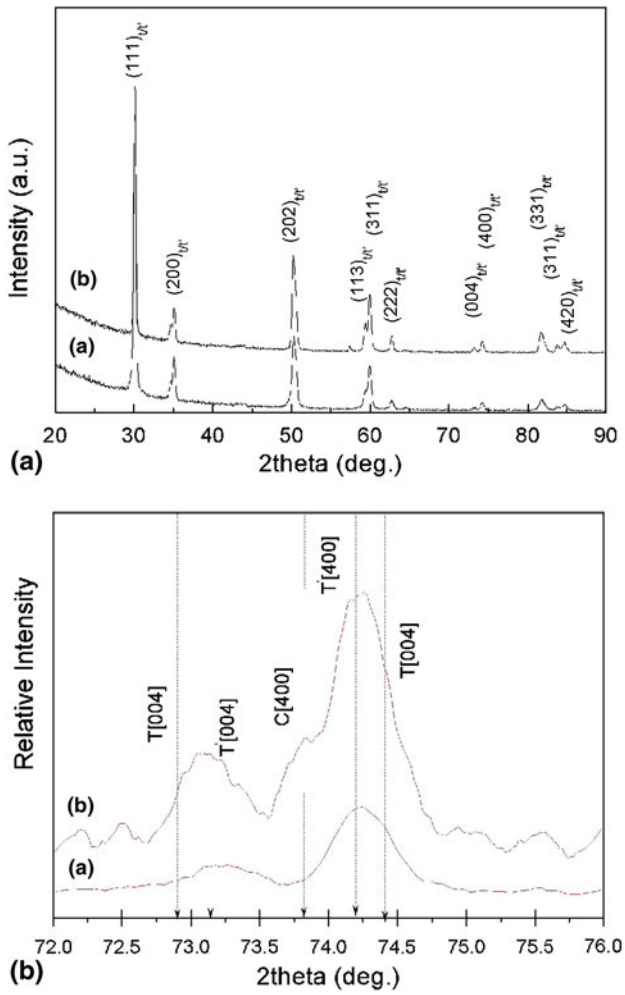

Fig. 11 XRD patterns of the nanostructured YSZ coatings: (a) as-sprayed and (b) after 500 cycles in 1473 K

shown in Fig. 10(b). The content of each phase in the coating are calculated roughly through the XRD diffraction peak intensity according to Eq 2 (Ref 31).

$$f_{t'} = I_{t'}/I_t + I_{t'} + I_c \quad \text{(Eq 2)}$$

$$f_c = I_{t'}/I_t + I_{t'} + I_c \quad \text{(Eq 3)}$$

$$f_t = I_t/I_t + I_{t'} + I_c \quad \text{(Eq 4)}$$

The content of t' phase and t phase in the as-sprayed coating is about 60 and 40%, respectively. After 500 cycles testing, the content of t' phase and t phase reduces to about 49 and 28%, respectively, while the content of c phase increases to 23% (Fig. 11b). It should be noted that phase transformation of tetragonal phase to monoclinic phase did not occur even after 500 thermal cycles. Phase transformation of YSZ did not cause damage to the integrity of the nano-TBC.

Sintering of TBCs is one of the very important properties affecting the lifetime of TBCs because residual stresses occur during the sintering process. The shrinkage of the nano-coating at 1523 K for 10 h is about 0.22% as

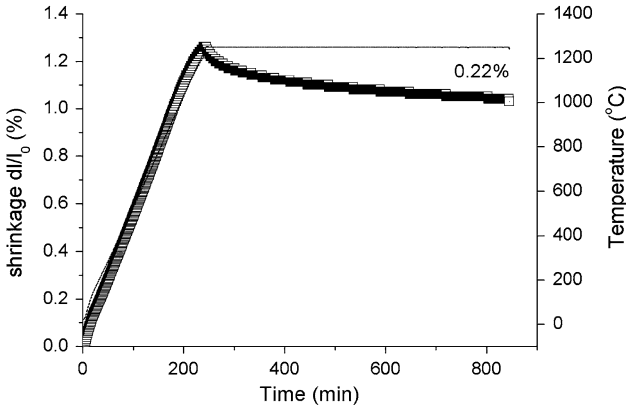

Fig. 12 Shrinkage of the free-standing YSZ nanostructured coating at 1523 K for 10 h

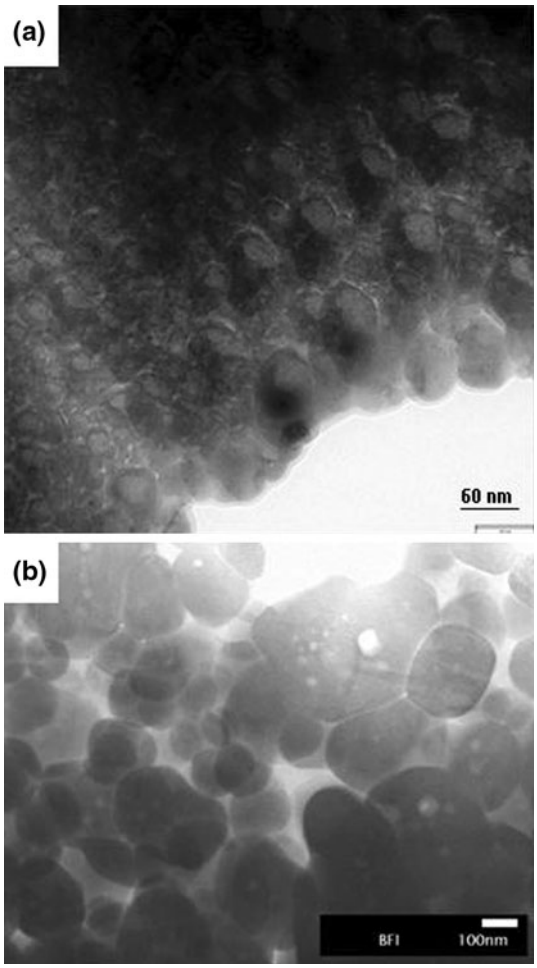

Fig. 13 TEM images of the as-sprayed coating (a) and the coating after 500 thermal cycles at 1523 K (b), showing densification and grain growth of the nano-coating after thermal cycling

shown in Fig. 12. For the conventional coating, the shrinkage at 1573 K for nearly 50 h is about 0.21% (Ref 32). This indicates that the conventional coating has a better sintering resistance than the nanostructured coating. Due to its microstructure features, the nanostructured coatings have higher compliance capacities and better thermal shock resistance than the conventional coating. Figure 13(a) and (b) shows the microstructure features of the as-sprayed nano-coating and the coating after 500 thermal cycles at 1523 K, respectively. For the as-sprayed coating, the grain size is in a range of 20-50 nm, while the grain size for the thermal cycled coating is larger than 100 nm. Also, the grains became dense after thermal cycling. Some globular pores remained in the grains due to sintering effect. Sintering resulted in material densification, accompanying with substantial grain growth in some regions, which was one of the reasons responsible for the failure of the nano-TBC.

4. Conclusions

The nanostructured YSZ TBC yielded a porosity of about 25% that was much higher than that of the conventional TBC, which is mainly attributed to the larger amount of intersplats in the coating. The thermal conductivity for the nano-coating was in the level of 0.8-1.1 W/m·K, about 40% lower than that for the conventional coating, indicating a better thermal insulation performance. The nano-TBC exhibited a thermal cycling lifetime of more than 500 cycles, whereas spallation failure of the conventional TBC occurred within 200 cycles. Failure of the nano-TBC was not caused by oxidation of the underlying bond coat and phase instability of YSZ coating. Accelerated sintering of the YSZ coating could be one of the main reasons for the failure of the nano-TBC.

Acknowledgments

This research is sponsored by the New Century Excellent Talents in University (NCET) and National Nature Science Foundation of China (NSFC, No. 50771009 and No. 50731001).

References

1. M. Gell, Application Opportunities for Nanostructure Materials and Coatings, *Mater. Sci. Eng.*, 1995, **204**(1-2), p 246-251
2. D. Zhu and R.A. Miller, Thermal Conductivity and Elastic Modulus Evolution of Thermal Barrier Coatings Under High Heat Flux Conditions, NASA TM-209069, NASA Glenn Research Center, Cleveland, OH, 1999
3. N.P. Padture, M. Gell, and E.H. Jordan, Thermal Barrier Coatings for Gas-Turbine Engine Application, *Science*, 2002, **296**, p 280-284
4. H. Chen and C.X. Ding, Nanostructured Zirconia Coating Prepared by Atmospheric Plasma Spraying, *Surf. Coat. Technol.*, 2002, **150**(1), p 31-36
5. A.L. Vasiliev, N.P. Padture, and X.Q. Ma, Coatings of Metastable Ceramics Deposited by Solution-Precursor, *Acta Mater.*, 2006, **54**(18), p 4913-4920
6. B. Liang, H.L. Liao, C.X. Ding, and C. Coddet, Nanostructured Zirconia-30vol.% Alumina Composite Coatings Deposited by Atmospheric Plasma Spraying, *Thin Solid Films*, 2005, **484**(1-2), p 225-231

7. R.A. Miller, Thermal Barrier Coatings for Aircraft Engines: History and Directions, *J. Therm. Spray Technol.*, 1997, **6**(1), p 35-42
8. Y. Zeng, S.W. Lee, L. Gao, and C.X. Ding, Atmospheric Plasma Sprayed Coatings of Nanostructured Zirconia, *J. Eur. Ceram. Soc.*, 2002, **22**(3), p 347
9. A.L. Vasiliev and N.P. Padture, Coatings of Metastable Ceramics Deposited by Solution-Precursor Plasma Spray: II. Ternary ZrO_2-Y_2O_3-Al_2O_3 system, *Acta Mater.*, 2006, **54**(18), p 4921-4928
10. H.B. Guo, S. Kuroda, and H. Murakami, Microstructures and Properties of Plasma-Sprayed Thermal Barrier Coatings, *J. Am. Ceram. Soc.*, 2006, **89**(4), p 1432-1439
11. H.B. Guo, R. Vaben, and D. Stöver, Thermophysical Properties and Thermal Cycling Behavior of Plasma Sprayed Thick Thermal Barrier Coatings, *Surf. Coat. Technol.*, 2005, **192**(1), p 48-56
12. H.B. Guo, H. Murakami, and S. Kuroda, Effect of Hollow Spherical Powder Size Distribution on Porosity and Segmentation Cracks in Thermal Barrier Coating, *J. Am. Ceram. Soc.*, 2006, **89**(12), p 3797-3804
13. M. Gell, Applying Nanostructured Materials to Future Gas Turbine Engines, *JOM*, 1994, **46**(10), p 30-34
14. R.S. Lima and B.R. Marple, Nanostructured YSZ Thermal Barrier Coatings Engineered to Counteract Sintering Effects, *Mater. Sci. Eng. A*, 2008, **485**(1-2), p 182-193
15. C.B. Liu, Z.M. Zhang, X.L. Jiang, M. Liu, and Z.H. Zhu, Comparison of Thermal Shock Behaviors Zirconia Thermal Barrier Coatings, *Trans. Nonferrous Met. Soc. China*, 2009, **19**(1), p 99-107
16. B. Liang and C.X. Ding, Thermal Shock Resistances of Nanostructured and Conventional Zirconia Coatings Deposited By Atmospheric Plasma Spraying, *Surf. Coat. Technol.*, 2005, **197**(2-3), p 185-192
17. W.Q. Wang, C.K. Sha, D.Q. Sun, and X.Y. Gu, Microstructural Feature, Thermal Shock Resistance and Isothermal Oxidation Resistance of Nanostructured Zirconia Coating, *Mater. Sci. Eng. A*, 2006, **424**(1-2), p 1-5
18. N. Wang, C. Zhou, S. Gong, and H. Xu, Heat Treatment of Nanostructured Thermal Barrier Coating, *Ceram. Int.*, 2007, **33**(6), p 1075-1081
19. C. Zhou, N. Wang, Z. Wang, S. Gong, and H. Xu, Thermal Cycling Life and Thermal Diffusivity of a Plasma-Sprayed Nanostructured Thermal Barrier Coating, *Scr. Mater.*, 2004, **51**, p 945-948
20. J. Wu, L.J. Zhu, F.H. Yuan, and X. Duan, Processing and Properties of Nanostructure YSZ Thermal Barrier Coatings on Superalloy K417G, *J. Surf. Eng. (Sinica)*, 2006, **5**, p 26-31
21. J. Wu, Hot-Corrosion Performances of Plasma Sprayed Nanostructure YSZ Thermal Barrier Coatings, Master Thesis, Shenyang Ligong University, 2007
22. H. Chen, Y. Zeng, and C.X. Ding, Microstructural Characterization of Plasma-Sprayed Nanostructured Zirconia Powders and Coatings, *J. Eur. Ceram. Soc.*, 2003, **23**(3), p 491-497
23. R.S. Lima, A. Kucuk, and C.C. Berndt, Integrity of Nanostructured Partially Stabilized Zirconia after Plasma Spray Processing, *Mater. Sci. Eng. A*, 2001, **313**(1-2), p 75-82
24. A.F. Cernuschi, S. Ahmaniemi, P. Vuoristo, and T. Mäntylä, Modeling of Thermal Conductivity of Porous Materials: Application to Thick Thermal Barrier Coatings, *J. Eur. Ceram. Soc.*, 2004, **186**, p 353-363
25. H.B. Guo, Y. Wang, L. Wang, and S.K. Gong, Thermo-Physical Properties and Thermal Shock Resistance of Segmented $La_2Ce_2O_7$/YSZ Thermal Barrier Coatings, *J. Therm. Spray Technol.*, 2009, **18**(4), p 665-671
26. R. Taylor, J.R. Brandon, and P. Morrell, Microstructure, Composition and Property Relationships of Plasma-Sprayed Thermal Barrier Coatings, *Surf. Coat. Technol.*, 1992, **50**(2), p 141-149
27. I.H. Jung, J.S. Moon, K.C. Song, and K.K. Bae, A Study of the Microstructure of Yttria-Stabilized Zirconia Deposited by Inductively Coupled Plasma Spraying, *J. Therm. Spray Technol.*, 2000, **9**(4), p 463-477
28. R. McPherson, A Review of Microstructure and Properties of Plasma Sprayed Ceramic Coatings, *Surf. Coat. Technol.*, 1989, **39-40**, p 173-181
29. J. Moon, H. Choi, H. Kim, and C. Lee, The Effects of Heat Treatment on the Phase Transformation Behavior of Plasma-Sprayed Stabilized ZrO_2 Coatings, *Surf. Coat. Technol.*, 2002, **155**(1), p 1-10
30. M. Leoni, R.L. Jones, and P. Scardi, Phase Stability of Scandia-Yttria-Stabilized Zirconia TBCs, *Surf. Coat. Technol.*, 1998, **108**, p 107-113
31. X.Q. Cao, Thermal Barrier Coatings Materials, July 6, 2007 (Changchun, China), Publisher of Science, 2007, p 189-190
32. C. Friedrich, R. Gadow, and T. Schirmer, Lanthanum Hexaaluminate-A New Material for Atmospheric Plasma Spraying of Advanced Thermal Barrier Coatings, *J. Therm. Spray Technol.*, 2001, **10**(4), p 592-598